J Physiol 588.1 (2010) pp 187–199

The Journal of Physiology

Elementary properties of $Ca_V1.3$ Ca^{2+} channels expressed in mouse cochlear inner hair cells

Valeria Zampini[1,2], Stuart L. Johnson[1], Christoph Franz[3], Neil D. Lawrence[4], Stefan Münkner[5,6], Jutta Engel[5,6], Marlies Knipper[3], Jacopo Magistretti[2], Sergio Masetto[2] and Walter Marcotti[1]

[1]*Department of Biomedical Science, University of Sheffield, Sheffield S10 2TN, UK*
[2]*Department of Physiological and Pharmacological Science, University of Pavia, Pavia 27100, Italy*
[3]*Department of Otolaryngology, Tübingen Hearing Research Centre (THRC), Laboratory of Molecular Physiology of Hearing, University of Tübingen, D-72076 Tübingen, Germany*
[4]*School of Computer Science, University of Manchester, Manchester M13 9PL, UK*
[5]*Institute of Physiology II and Tübingen Hearing Research Centre (THRC), University of Tübingen, D-72076 Tübingen, Germany*
[6]*Department of Biophysics, Saarland University, 66421 Homburg/Saar, Germany*

Mammalian cochlear inner hair cells (IHCs) are specialized to process developmental signals during immature stages and sound stimuli in adult animals. These signals are conveyed onto auditory afferent nerve fibres. Neurotransmitter release at IHC ribbon synapses is controlled by L-type $Ca_V1.3$ Ca^{2+} channels, the biophysics of which are still unknown in native mammalian cells. We have investigated the localization and elementary properties of Ca^{2+} channels in immature mouse IHCs under near-physiological recording conditions. $Ca_V1.3$ Ca^{2+} channels at the cell pre-synaptic site co-localize with about half of the total number of ribbons present in immature IHCs. These channels activated at about −70 mV, showed a relatively short first latency and weak inactivation, which would allow IHCs to generate and accurately encode spontaneous Ca^{2+} action potential activity characteristic of these immature cells. The $Ca_V1.3$ Ca^{2+} channels showed a very low open probability (about 0.15 at −20 mV: near the peak of an action potential). Comparison of elementary and macroscopic Ca^{2+} currents indicated that very few Ca^{2+} channels are associated with each docked vesicle at IHC ribbon synapses. Finally, we found that the open probability of Ca^{2+} channels, but not their opening time, was voltage dependent. This finding provides a possible correlation between presynaptic Ca^{2+} channel properties and the characteristic frequency/amplitude of EPSCs in auditory afferent fibres.

(Received 29 September 2009; accepted after revision 11 November 2009; first published online 16 November 2009)
Corresponding author W. Marcotti: Department of Biomedical Science, University of Sheffield, Sheffield S10 2TN, UK. Email: w.marcotti@sheffield.ac.uk

Abbreviations APs, action potentials; EPSCs, excytatory postsynaptic currents; IHCs, inner hair cells; P, postnatal day; P_o, open channel probability; RRP, readily releasable pool.

Introduction

In adult animals the auditory organ contains a specialized neuroepithelium of sensory hair cells responsible for converting acoustic stimuli into an electrical signal via the activation of mechano-sensitive transducer channels (Fettiplace & Hackney, 2006). Inner hair cells (IHCs), the primary sensory receptors of the mammalian cochlea, relay acoustic signals with remarkable acuity and temporal precision to the brain via auditory afferent fibres (Fuchs, 2005). However, before the onset of hearing at around postnatal day 12 in most rodents, IHCs fire spontaneous Ca^{2+} action potentials thought to control the remodelling of immature synaptic connections within the cochlea (Kros *et al.* 1998). The encoding of these physiological responses largely depends on the transfer characteristics of IHC ribbon synapses (Fuchs, 2005). Synaptic ribbons are specialized organelles able to tether a large number of synaptic vesicles at the cell's active zones (Sterling & Matthews, 2005). Their presence at synapses has been linked with the ability of sensory cells to mediate high rates of sustained synaptic transmission, coordinated release of multiple vesicles (Sterling & Matthews, 2005; Goutman & Glowatzki, 2007; Neef *et al.* 2007) and temporally precise transfer of information (Wittig & Parsons, 2008).

V. Zampini and S. L. Johnson contributed equally to this work.

DOI: 10.1113/jphysiol.2009.181917

Synaptic vesicle fusion at IHC presynaptic active zones is controlled by Ca^{2+} entry through L-type ($Ca_V1.3$) Ca^{2+} channels (Brandt *et al*. 2003) in response to either action potentials in immature or sound-induced graded receptor potentials in adult animals. In order for hair cells to follow these physiological signals, the macroscopic $Ca_V1.3$ Ca^{2+} current activates very rapidly and shows little inactivation (Johnson & Marcotti, 2008; Grant & Fuchs, 2008). Moreover, the rapid rise and fall of intracellular Ca^{2+} transients, essential for temporal coding in adult animals, is ensured by an efficient Ca^{2+} buffering system (Roberts, 1993; Hackney *et al*. 2005; Johnson *et al*. 2008). Reliable synaptic transfer of the different immature and adult physiological signals also requires developmental changes in the Ca^{2+} sensitivity of the IHC synaptic machinery (Beutner & Moser, 2001; Johnson *et al*. 2005, 2008, 2009). At present, the active zone topography and mechanisms underlying multivesicular release at IHC ribbon synapses (Glowatzki *et al*. 2008) and the elementary properties of $Ca_V1.3$ Ca^{2+} channels in native mammalian cells (Catterall *et al*. 2005) are unknown. The biophysical properties of these Ca^{2+} channels are likely to be crucial to understanding the functional coupling between Ca^{2+} entry and vesicle release, especially when considering that one Ca^{2+} channel, or a small number of them, might govern exocytosis at IHC ribbon synapses (Brandt *et al*. 2005). Using near-physiological experimental conditions, we have investigated the elementary properties of $Ca_V1.3$ Ca^{2+} channels in pre-hearing mouse IHCs.

Methods

Tissue preparation for electrophysiological recording

Apical coil inner hair cells (IHCs, $n = 84$) from C57B mice were studied in acutely dissected organs of Corti from postnatal day 5 (P5) to P10, where the day of birth is P0. IHCs were from the apical coil of the cochlea, which corresponds to a frequency range of 0.8–3.0 kHz in adult mice (Ehret, 1975). Mice were killed by cervical dislocation in accordance with UK Home Office regulations. Cochleae were viewed using an upright microscope (Leica DMLFS, Germany). Prior to patch seal, the basolateral surface of IHCs was exposed using a suction pipette filled with a normal extracellular solution (in mM): 135 NaCl, 5.8 KCl, 1.3 $CaCl_2$, 0.9 $MgCl_2$, 0.7 NaH_2PO_4, 5.6 D-glucose, 10 Hepes-NaOH. Sodium pyruvate (2 mM), amino acids and vitamins were added from concentrates (Fisher, UK). The pH was adjusted to 7.5. For single Ca^{2+} channel recordings trypsin (0.3–1 mg ml^{-1}) was very briefly and topically applied onto IHCs prior attempting to seal (higher trypsin concentrations were not used because at body temperature it caused the cells to deteriorate).

Electrophysiological recording

All patch clamp recordings were performed near body temperature (35–37°C) using an Axopatch 200B (Molecular Devices, USA) and an Optopatch (Cairn Research Ltd, UK) amplifier. Data were acquired using pCLAMP software and a Digidata analog-to-digital converter (Molecular Devices).

For single Ca^{2+} channel recordings, patch pipettes were made from borosilicate glass capillaries (Harvard Apparatus Ltd, UK), fire-polished (resistance in the bath: 7–12 MΩ; seal resistance > 20 GΩ) and coated with surf wax (Mr Zoggs SexWax, USA) to minimize the fast electrode capacitative transient. Patch pipettes contained the following solution (in mM): 5 $CaCl_2$, 102 CsCl, 10 Hepes-KOH, 15 4-aminopyridine and 40 TEA (pH 7.5). In some experiments 5 or 70 mM Ba^{2+} was used instead of 5 mM Ca^{2+}. Apamin (300 nM: Merck Biosciences, UK), niflumic acid (50 μM: Sigma, UK) and BayK 8644 (5 μM: Sigma) were added to the pipette solution. Stock solutions of niflumic acid and BayK 8644 were prepared in DMSO and stored at −20°C (final dilution 1:2000). During the majority of recordings, the membrane potential of IHCs was zeroed by superfusing a high-K^+ extracellular solution (Zampini *et al*. 2006) containing (in mM): 140 KCl, 0.2 $CaCl_2$, 6.2 $MgCl_2$, 0.7 NaH_2PO_4, 5.6 D-glucose, 15 Hepes-KOH (pH = 7.5). In three experiments, normal high-Na^+ extracellular solution was used in order to measure the single Ca^{2+} channel current at the IHCs resting membrane potential (see red dot in Fig. 3*D*). Data were filtered at 2 or 5 kHz (4-pole Bessel) and sampled at 20 or 50 kHz. In a very few cases, current traces were additionally filtered offline at 1 kHz (8-pole Bessel). Membrane potentials were corrected for the liquid junction potential (LJP: +3 mV in 5 mM Ca^{2+} or 5 mM Ba^{2+}; −5 mV in 70 mM Ba^{2+}).

Whole-cell recordings were performed using soda glass capillaries (resistance 2–3 MΩ) coated with surf-wax and filled with (in mM): 106 caesium glutamate, 20 CsCl, 3 $MgCl_2$, 1 EGTA–CsOH, 5 Na_2ATP, 0.3 Na_2GTP, 5 Hepes-CsOH, 10 sodium phosphocreatine (pH 7.3). Inward currents were recorded in isolation by superfusing IHCs with K^+ channel blockers (TEA: 30 mM, 4-aminopyridine: 15 mM, apamin: 300 nM) added to the above normal extracellular solution. BayK 8644 (5 μM) and 5 mM Ca^{2+} were also used extracellularly to mimic the single-channel experimental conditions. Recordings were filtered at 5 or 10 kHz (8-pole Bessel) and sampled at 50 or 100 kHz. Linear leak conductance was subtracted off-line using Clampfit (g_{leak}: 1.7 ± 0.1 nS, $n = 40$: usually calculated between −84 mV and −74 mV, as the Ca^{2+} current activates positive to or at around −70 mV) and membrane potentials were corrected for residual series resistance (R_s: 4.8 ± 0.3 MΩ, $n = 41$) and LJP (−11 mV). The voltage clamp time constant was 41 ± 3 μs (product of R_s and membrane capacitance (C_m): 8.5 ± 0.2 pF).

Immunocytochemistry

Immature mouse (P6 and P7) cochleae were isolated, fixed, cryosectioned and stained as described (Knipper *et al.* 2000; Knirsch *et al.* 2007). Animals were killed by exposure to a rising concentration of CO_2 gas in accordance with the ethical guidelines approved by the University of Tübingen and the Tierschutzgesetz (Germany). Apical IHCs were stained using rabbit polyclonal anti-$Ca_V1.3$ (Alomone Labs, 1:50) and mouse monoclonal anti-CtBP2/RIBEYE (BD Transduction Laboratories, CA, USA; 1:50) antibodies. Primary antibodies were detected with Cy3-conjugated (Jackson ImmunoResearch Laboratories, USA) or Alexa Fluor 488-conjugated antibodies (Molecular Probes, USA). Sections were embedded with Vectashield mounting medium with DAPI (Vector Laboratories, USA). Sections were viewed using an Olympus AX70 microscope equipped with epifluorescence illumination ($\times 100$ objective, NA = 1.35) and a motorized z-axis. Images were acquired using a CCD camera and the imaging software Cell^F (OSIS GmbH, Münster, Germany). For $Ca_V1.3$ and CtBP2/RIBEYE immunopositive spot counting, cryo-sectioned cochleae were imaged over a distance of 8 μm with the complete coverage of the IHC nucleus and beyond in an image-stack along the z-axis (z-stack). Typically z-stacks consisted of 30 layers with a z-increment of 0.276 μm, for each layer one image per fluorochrome was acquired. z-stacks were 3-dimensionally deconvoluted using Cell^F's RIDE module with the Nearest Neighbour algorithm (OSIS GmbH, Münster, Germany). Panels *A–C*, *E* and *F* in Fig. 1 are composite images, which represent the maximum intensity projection over all layers of the z-stack. Figure 1*D* is a single layer image at the nuclear level from z-stack-deconvoluted pictures.

The theoretical resolution (Abbe's law of diffraction of monochromatic light) of this system in x- and y-axes was estimated to be 211 nm for Cy3 (emission maximum $E_{max} = 570$ nm) and 192 nm for Alexa 488 ($E_{max} = 517$ nm), respectively. The deconvolution process in z-axis is likely to improve the resolution further since it reduces the object size in the x- and y-axes for a projected z-stack, due to the reduction of blur in both axes. However, in order to better define the actual resolution of our system, we measured the pixel intensity of beads with known diameter (175 nm − green light emission; PS-Speck Microscope Point Source Kit, Molecular Probes). From each bead we generated a diffraction pattern intensity profile, fitted the data with the Airy function and measured the width at half-maximum (257 ± 4 nm, $n = 7$), which suggests an 82 nm (or 46%) increase in the true bead size under our experimental conditions. The diameter of ribbons we measured from immature IHCs was on average 376 nm (using Alexa 488 as secondary antibody), which is in the range of that previously reported by transmission electron microscopy (about 300 nm: Sobkowicz *et al.* 1982) and larger than the above diffraction pattern of the beads. As a conservative approach we used a minimum overlap between ribbon and Ca^{2+} channel immunospots of 46% as a criterion for co-localization. This would probably underestimate the co-localized clusters, since the spread of the diffraction is constant (does not change relative to the object's size). However, we did not see a ribbon overlap with Ca^{2+} spots of less than 50%.

Data analysis

Single Ca^{2+} channel analysis was performed as previously described (Zampini *et al.* 2006) using Clampfit (Molecular Devices) and Origin (OriginLab, USA). Briefly, leak and uncompensated capacitive currents were corrected by subtracting average episodes without channel activity (null sweeps) from the active sweeps. Event detection was performed with the 50% threshold detection method with each transition visually inspected before being accepted. Idealized traces were used to calculate single-channel amplitude distribution (event duration > 0.34 ms), open probability (P_o) and open and closed time histograms. Distributions were fitted with a single or double Gaussian function (current amplitude) or multiple exponentials (dwell times). The P_o of Ca^{2+} channels as a function of voltage (Fig. 3*F*) was fitted using a first-order Boltzmann equation:

$$P_o = P_{o(min)} + \frac{(P_{o(max)} - P_{o(min)})}{\left(1 + \exp\left(\frac{V - V_{1/2}}{S}\right)\right)} \quad (1)$$

where P_o represents the mean open probability, $P_{o(min)}$ and $P_{o(max)}$ are the minimum and maximum P_o, V is voltage, $V_{1/2}$ is the voltage at which P_o is half-maximum and S is the voltage sensitivity. P_o was corrected for the number of channels present in the patch.

The number of Ca^{2+} channels (N) in the patch recordings was estimated as the largest number of overlapping channels at membrane potentials where P_o was highest. Because the maximum P_o was very low, the following algorithm was used to estimate the likelihood of overlapping events in those patches without superimposed openings (Plummer *et al.* 1989): $P_2(T) = 1 - (1 - P_{2o})^{T/t}$, where $P_2(T)$ is the cumulative probability of observing superimposed openings due to the activity of two identical channels over the total observation time T, P_{2o} is the overall probability of finding two simultaneous openings, and t is twice the mean open time.

The total number of Ca^{2+} channels expressed in IHCs was estimated using the following equation:

$$N = \frac{I}{iP_o} \quad (2)$$

where N is the total number of channels, I is the size of the macroscopic Ca^{2+} current measured using 500 ms voltage steps, i is the single-channel current size and P_o the open channel probability.

To calculate the single-channel open and closed times at each membrane potential (Fig. 4), data from IHCs were pooled to obtain a distribution of dwell times on a log scale (20 bins/decade) with no normalization of the number of observations for bin amplitude (Sigworth & Sine, 1987). The plots obtained were interpolated, using the maximum-likelihood method, with the following transform of the sum of n (two or three) exponential functions (Sigworth & Sine, 1987):

$$f(t) = \sum_{i=1}^{n} P_i e^{[\ln(t)-\ln(\tau_i)-e^{\ln(t)-\ln(\tau_i)}]} \quad (3)$$

where P_i and τ_i are the relative area and time constant of the i^{th} component of the distribution. When more Ca^{2+} channels were present in the patch, time constants were calculated by excluding sweeps containing multiple openings.

Theoretical mean dwell times ($\bar{\tau}$), used to estimate P_o in Fig. 4*E*, were derived from the exponential fitting functions according to the relation:

$$\bar{\tau} = \sum P_i \tau_i \quad (4)$$

where P_i has the same meaning as above. Open channel probability was also estimated from the mean open and closed times (calculated according to eqn (4)) using the following function:

$$P_o = \frac{\bar{\tau}_o}{(\bar{\tau}_o + \bar{\tau}_c)} \quad (5)$$

The first latency distribution was investigated by measuring the time interval between 63% of the capacitative transient decay (τ: 0.14 ± 0.07 ms, $n = 5$) and the first opening. These values were corrected for the number of channels in the patch (Colquhoun & Hawkes, 1987). The number of events used for this analysis was smaller than those used for the dwell times, since only the time to the first opening from each trace could be used. The distribution of the first latency was analysed using log–log plots (McManus *et al.* 1987). Lower and upper bin limits were first set according to a logarithmic scale (6.64 bins per decade). After binning, the number of events (n) was divided by the corresponding bin width (δt_i), and the natural logarithm of $n_i/\delta t_i$ ratio was calculated. These values were plotted as a function of $x = \ln t$ to construct log–log frequency distribution graphs (see Fig. 5). Exponential fitting of log–log histograms was performed by applying the following double-logarithmic transform of a sum of exponential equations (McManus *et al.* 1987):

$$y = \ln\left\{\sum_{j=1}^{m} \frac{W_j}{\tau_j} \exp[-\exp(x - x_{oj})]\right\} \quad (6)$$

where $x_{oj} = \ln\tau_j$, and W_j and τ_j are the weight coefficient and time constant, respectively, for each exponential component. The above fits were based on a minimum χ^2 method.

The current–voltage curve shown in Figs 3*E* and 6*A* was obtained using the following equation:

$$I = (g_{max}(V - V_{rev}))\left(g_{max} + \frac{g_{min} - g_{max}}{\left(1 + \exp\left(\frac{V_{1/2}-V}{S}\right)\right)}\right) \quad (7)$$

where I is the current, V_{rev} is the reversal potential, g_{max} and g_{min} are the maximum and minimum chord conductance and the other parameters are as in eqn (1).

The activation curves of the macroscopic Ca^{2+} current (Fig. 3*F*) were obtained from the normalized chord conductance (Zidanic & Fuchs, 1995; Johnson *et al.* 2005) using the reversal potential of +48 mV (Johnson *et al.* 2005), and approximated by a first-order Boltzmann equation (see eqn (1)). The activation kinetics of the macroscopic I_{Ca} (Fig. 6*C*) were approximated using the following equation:

$$I(t) = I_{max}\left(1 - \exp\left(\frac{-t}{\tau}\right)\right)^{\alpha} \quad (8)$$

where $I(t)$ is the current at time t, I_{max} is the peak I_{Ca}, τ is the time constant of activation and α was fixed at 2, which gave a better fit than a power of 3 (as previously described: Johnson *et al.* 2005; Johnson & Marcotti, 2008), consistent with a Hodgkin–Huxley model with two opening gating particles (Hodgkin & Huxley, 1952).

Statistical analysis

Statistical comparisons of means were made by Student's two-tailed t test or, for multiple comparisons, analysis of variance ANOVA (one-way followed by the Tukey post test; two-way followed by the Bonferroni post test). Mean values are quoted ± S.E.M. where $P < 0.05$ indicates statistical significance.

Results

Ca^{2+} channel localization in immature IHCs

The distribution of $Ca_V1.3$ channels within immature IHCs was investigated using immunolabelling experiments (Fig. 1). Calcium channel clusters were not only found at the IHC presynaptic region, as for post-hearing

IHCs (Fig. 1*F*: see also Brandt *et al.* 2005; Meyer *et al.* 2009), but also in their neck region (Fig. 1*A*, *C* and *D*). Although the total number of immunopositive $Ca_V1.3$ spots measured in eight P7 mouse IHCs was 80 ± 13 (Fig. 1*G*), only about 70% of them (56 spots) were associated with the plasma membrane (Fig. 1*D*). Some of these Ca^{2+} spots (15 ± 3) co-localized with synaptic ribbons found in the basal pole of immature IHCs (31 ± 4 ribbons: Fig. 1*E* and *G*). Co-localization was evaluated using *z*-stack images (see Methods for details). The finding that only about 50% of ribbons were co-localized with Ca^{2+} channels in immature IHCs was surprising since in adult cells all, or the majority of them, co-localized with Ca^{2+} channel spots (Fig. 1*F*: see also Brandt *et al.* 2005). Such a difference could indicate that the synaptic machinery from early postnatal

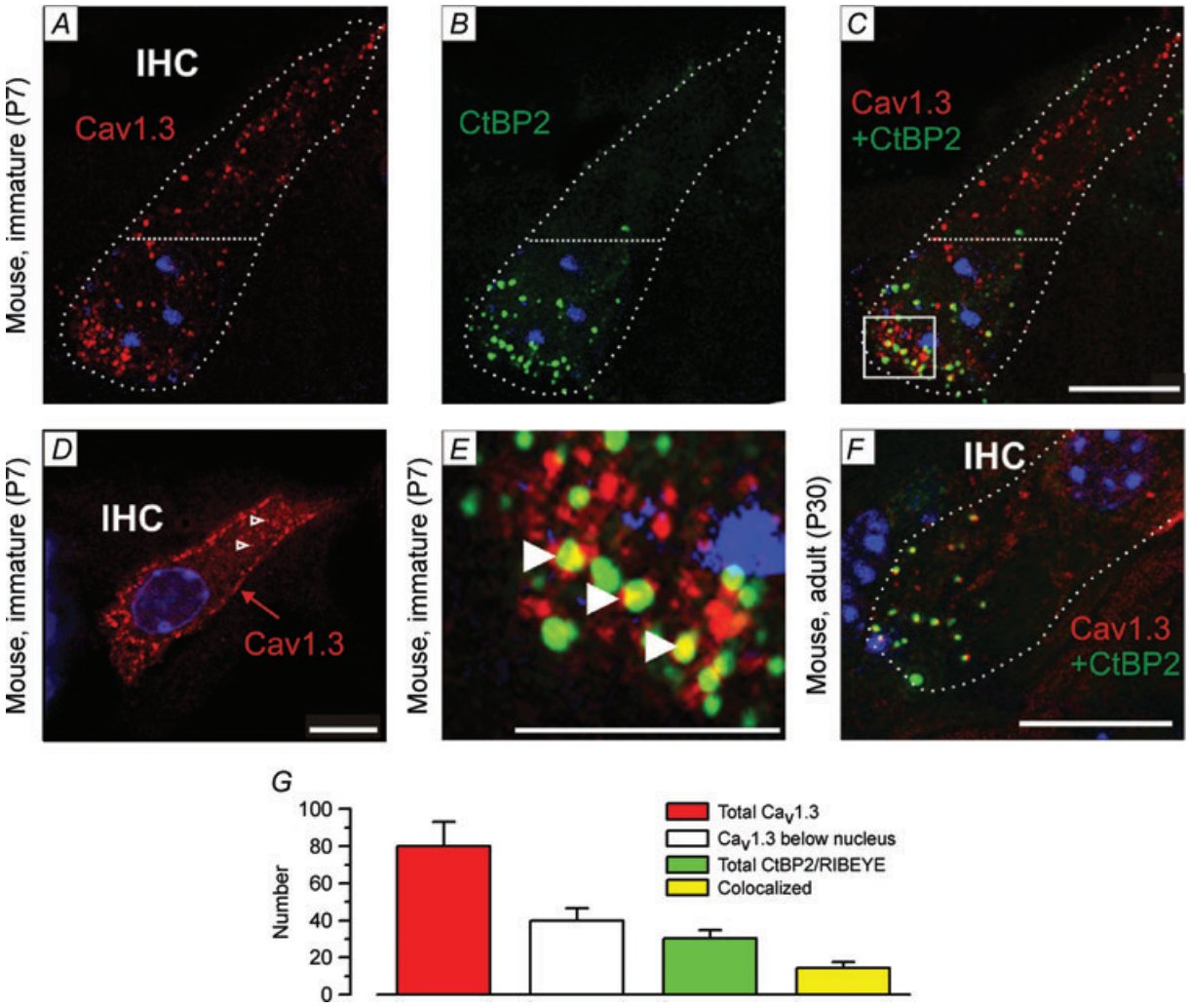

Figure 1. Distribution of $Ca_V1.3$ and CtBP2/RIBEYE in immature mouse IHCs
A–C, an apical IHC from a P7 mouse immunostained for the $Ca_V1.3$ Ca^{2+} channel (*A*, red) and ribbon marker CtBP2/RIBEYE (*B*, green), merged image shown in *C*. Sparse dotted lines delineate IHCs. The region below the horizontal dotted line at the IHC nuclear level indicates the position for all single Ca^{2+} channel recordings shown in the following figures. Note that $Ca_V1.3$ is distributed over the whole surface area of the IHC (*A*), whereas CtBP2 is exclusively localized at its basal pole (*B*). *D*, single layer image from a P7 IHC showing that most Ca^{2+} channel spots delineate the boundaries (plasma membrane). *E*, magnification of the boxed area in *C* (examples of co-localization in yellow is indicated by filled arrowheads). *F*, basal region of an adult (P30) IHC showing co-localization between CtBP2/RIBEYE and Ca^{2+} channel immunopositive spots. Images in panels *C, E* and *F* represent the maximum intensity projection over all layers of the *z*-stack. *D* represents a single layer image at the nuclear level from *z*-stack deconvoluted images. Nuclei in *A–F* were stained with DAPI (blue); note that after deconvolution mainly nucleoli are visible. Scale bar in *A–D* and *F* indicates 10 μm; in *E* 5 μm. *G*, total number of immunopositive spots for $Ca_V1.3$ (red bar), total number of $Ca_V1.3$ positive spots below the IHC's nuclei (white bar) and CtBP2/RIBEYE (green bar) measured from eight P7 immature IHCs. Note that 70% of these Ca^{2+} spots were associated with the plasma membrane and that some CtBP2/RIBEYE spots were seen to co-localize (yellow bar) with $Ca_V1.3$ immunospots.

cells has yet to fully mature, as recently shown for proteins involved in ribbon synapse formation in immature photoreceptor cells (Regus-Leidig *et al*. 2009). Nevertheless, the above findings show that only a small proportion (∼27%: 15 out of 56 $Ca_V1.3$ spots in the membrane) of Ca^{2+} channels expressed in these immature cells are directly associated with presynaptic active zones, assuming a similar distribution of Ca^{2+} channels among the immunopositive spots. However, this is not surprising since Ca^{2+} channels in immature IHCs also have a purely electrical function in the generation of action potentials (APs: Marcotti *et al*. 2003*b*) and activation of the small conductance Ca^{2+}-activated K^+ current SK2, which has a crucial role in the AP repolarization (Marcotti *et al*. 2004; Johnson *et al*. 2007). The specificity of the $Ca_V1.3$ antibody was verified by performing experiments on $Ca_V1.3$ knockout mice (Platzer *et al*. 2000) and pre-incubating the antibody with the antigenic peptide (see Supplemental Fig. 1, available online only).

Single Ca^{2+} channel recordings were only performed on the basal pole of IHCs (from around the level of the horizontal dotted line and below in Fig. 1*A*–*C*), which contains roughly 50% of the total Ca^{2+} channel spots associated with the membrane. At first, the success rate for observing single Ca^{2+} channel openings was extremely low (less than 3%), most likely because of channels being masked by afferent terminals contacting immature IHCs (Pujol *et al*. 1998). In order to improve the recording success rate, IHCs were very briefly and topically perfused with trypsin prior to attempting to seal. After this procedure, 43 out of 313 patches were successful in that they showed Ca^{2+} channel activity. For the only single Ca^{2+} channel activity recorded without trypsin, where a current–voltage relation for the Ca^{2+} current (I_{Ca}) could be measured, the channel conductance did not differ from those obtained following enzyme treatment (data not shown). This finding is consistent with previous observations showing that the biophysical properties of the single-channel and macroscopic L-type Ca^{2+} currents recorded from enzymatic-isolated vestibular hair cells (Prigioni *et al*. 1992; Rodriguez-Contreras & Yamoah, 2001) were similar to those measured from slice preparations (Russo *et al*. 2003; Zampini *et al*. 2006).

Following the brief topical enzymatic treatment of the IHC to be patched, the majority of the successful patches (77%) contained one (Fig. 3*A*) or two Ca^{2+} channels (Fig. 3*B*) and the rest contained three or four. We never recorded from membrane patches containing a large number of Ca^{2+} channels such as those previously described in bullfrog auditory hair cells (Rodriguez-Contreras & Yamoah, 2001). One possible explanation for this discrepancy is that the mild enzymatic treatment used for the experiments was not sufficient to remove the afferent terminals completely and unmask all Ca^{2+} channels.

Due to the presence of extrasynaptic Ca^{2+} channels within the IHC basal pole (see the single-channel recording area below the horizontal dotted line: Fig. 1), it is very likely that some of the patches we recorded would have contained channels located outside the cell active zones. Nevertheless, current evidence from lower vertebrate hair cells suggests that the biophysical properties of L-type $Ca_V1.3$ channels appear homogeneous irrespective of their location within a cell (Rodriguez-Contreras & Yamoah, 2001; Zampini *et al*. 2006).

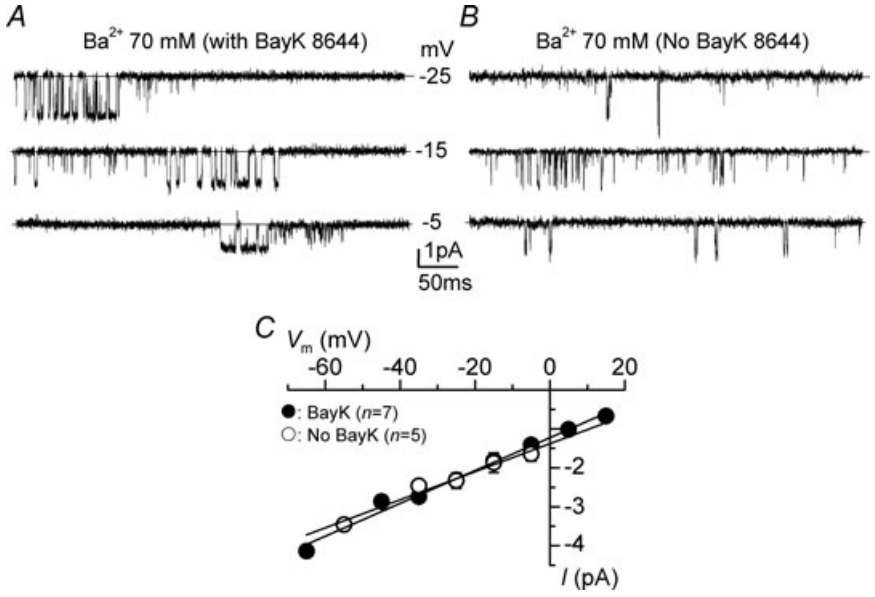

Figure 2. Effect of BayK 8644 on the unitary Ca^{2+} channel current
A and *B*, representative unitary currents recorded in immature IHCs in the presence of 70 mM Ba^{2+} with (*A*) and without (*B*) BayK 8644 in the pipette solution. *C*, *I–V* from single-channel experiments in 70 mM Ba^{2+} with (between 1 and 7 patches were used for each voltage step, P8–P9) and without (1–5 patches; P7–P10) BayK 8644. In this and the following figures the number of patches corresponds to the number of IHCs investigated and recordings were performed at 35–37°C.

Unitary current and open probability of $Ca_V1.3$ Ca^{2+} channels in immature IHCs

Single Ca^{2+} channel currents were recorded from P5–P10 IHCs. The majority of the experiments were performed at body temperature and using near-physiological Ca^{2+} concentrations (5 mM) and BayK 8644 (5 μM). The use of BayK 8644 was essential when working at body temperature since in its absence the majority of single-channel openings were not resolved and the apparent sub-conductive open states became very frequent. This behaviour was observed even when the signal-to-noise ratio of the recordings was enhanced by increasing the single-channel current with 70 mM Ba^{2+} (Fig. 2*A* and *B*). Although BayK 8644 is known to produce longer Ca^{2+} channel openings, it does not significantly affect the single Ca^{2+} channel amplitude (Hess *et al.* 1984), as also shown in Fig. 2. The slope conductance of the single Ca^{2+} channel current (Fig. 2*C*) recorded with BayK 8644 (39.0 ± 1.8 pS, $n = 7$) in the pipette solution was similar to that measured in its absence (36.8 ± 3.3 pS, $n = 5$). In the presence of 5 mM Ca^{2+}, unitary $Ca_V1.3$ Ca^{2+} currents were observed as rare openings at most hyperpolarized membrane potentials that became more frequent with depolarization (Fig. 3*A*). Sub-conductive states were rarely observed in this condition and accounted for less than 1% of the conductive state (data not shown). The analysis of ensemble-average single Ca^{2+} channel currents showed a fast activation time constant and a slow time-dependent inactivation (Fig. 3*C*: $\tau = 0.1$ ms and $\tau = 771$ ms, respectively), consistent with that of the macroscopic Ca^{2+} current (Marcotti *et al.* 2003*b*). The single-channel current–voltage (*I–V*) relation was linear (Fig. 3*D*) with an average slope conductance of 14.4 pS ($n = 9$).

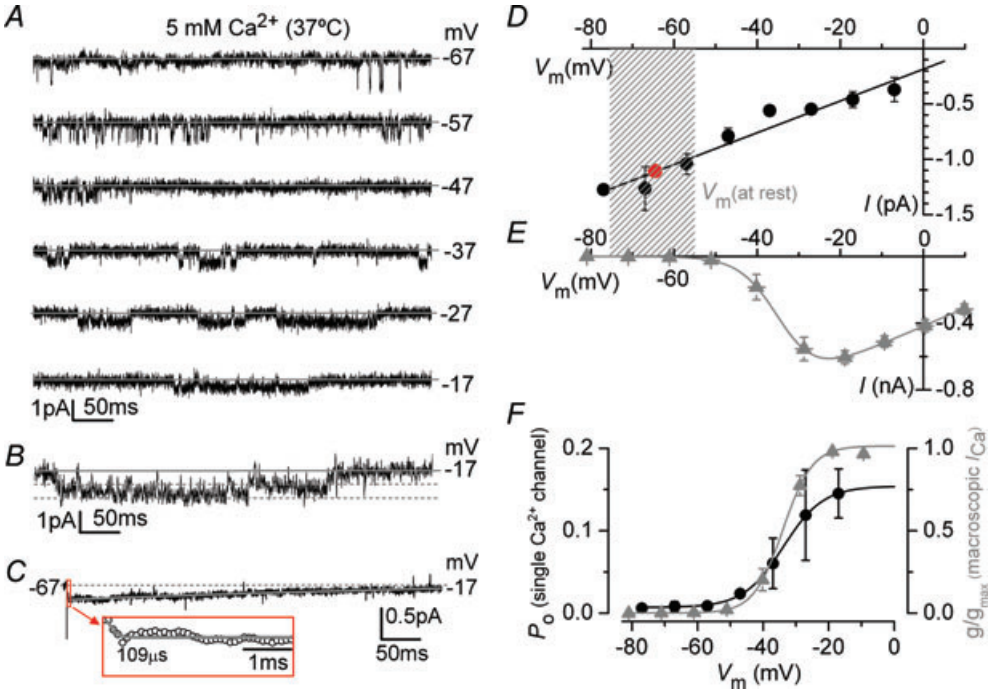

Figure 3. Unitary $Ca_V1.3$ L-type Ca^{2+} channel currents
A, representative unitary currents (500 ms recordings) from IHCs at membrane patch potentials shown next to the traces using 5 mM Ca^{2+} and BayK 8644. Grey lines indicate the channel closed state. *B*, current recordings indicating the presence of a cluster of two Ca^{2+} channels. Dashed lines indicate the main open current levels. *C*, ensemble-averaged current at −17 mV derived from 130 active sweeps from 6 IHCs. Holding potential = −67 mV. The inset shows a fit to the current onset using eqn (8) and for clarity, one of every two data points is shown. *D*, average *I–V* from single-channel currents ($2 \leq n \leq 6$ patches for each voltage; $n = 9$, P5–P8). Shaded area represents the resting membrane potential of immature IHCs (Marcotti *et al*. 2003*a*). The red dot indicates the elementary current size recorded in normal Na^+ extracellular solution at the cell resting potential (-1.1 ± 0.1 pA, $n = 3$). *E*, average *I–V* of the macroscopic Ca^{2+} current in P7 IHCs ($n = 8$) elicited using depolarizing voltage steps in 10 mV increments (500 ms in duration) from −81 mV. *F*, voltage-dependent activation of the macroscopic I_{Ca} (grey triangles) obtained by plotting the normalized chord conductance against the different membrane potentials. The continuous line is the fit obtained using a first-order Boltzmann equation (see Methods): $g_{max} = 9.0$ nS, $V_{1/2} = -34.0$ mV, $S = 4.5$ mV. Black circles show the mean open probability (P_o) of single Ca^{2+} channels at different membrane potentials ($1 \leq n \leq 4$ patches, $n = 5$, P5–P8). Data were fitted with a Boltzmann equation with parameters of: $P_{o(min)} = 0.007$; $P_{o(max)} = 0.154$; $V_{1/2} = -33.9$ mV; $S = 6.1$ mV. Note that the maximal individual P_o value measured at depolarized membrane potentials was 0.23.

Remarkably, single Ca^{2+} channel activity was detectable at very negative potentials (from about −70 mV), which corresponds to the resting membrane potential for these immature IHCs (from −50 mV to −70 mV: Marcotti *et al.* 2003*a*). At around this potential the single-channel current size was about 1.1 pA in both high K^+ and normal high Na^+ (red filled circle: Fig. 3*D*) extracellular solutions. In the same voltage range, about 1% (defined as percentage of g_{max}) of the macroscopic Ca^{2+} current was available (Fig. 3*E* and *F*, grey triangles).

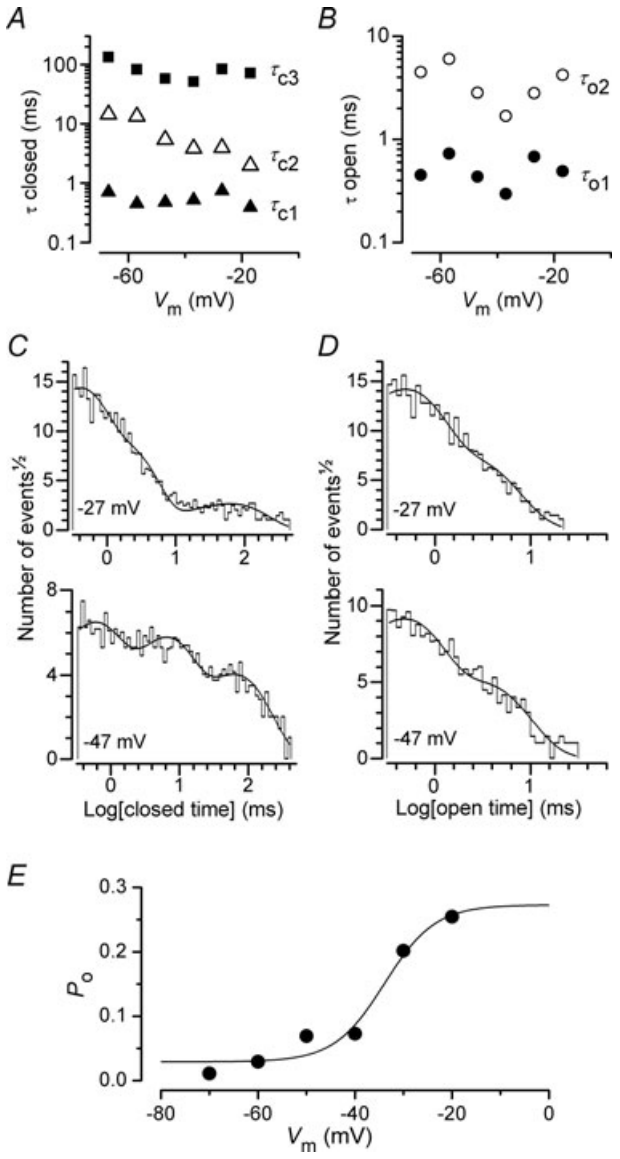

Figure 4. Closed and open time constants of unitary $Ca_V1.3$ Ca^{2+} currents
A and *B*, closed (τ_{c1}, τ_{c2} and τ_{c3}) and open (τ_{o1} and τ_{o2}) time constants, respectively, as a function of membrane patch potential derived from fitting the dwell-time distributions using the sum of two or three exponentials (eqn (3); $1 \leq n \leq 3$ patches for each voltage; $n = 6$). *C* and *D*, examples of closed and open time distributions, respectively, calculated at membrane potentials of −27 mV and −47 mV. Data are displayed on a log/linear scale (20 bins/decade) and fitted using eqn (3) with three (*C*) or two (*D*) exponentials. *E*, voltage dependence of the Ca^{2+} channel opening probability obtained by applying eqns (4) and (5) (see Methods), and using time constants from the above open- and closed-time distributions (see also Table 1). Data were fitted with a Boltzmann equation with parameters of: $P_{o(min)} = 0.03$; $P_{o(max)} = 0.27$; $V_{1/2} = -33.9$ mV; $S = 5.2$ mV.

The single Ca^{2+} channel open probability (P_o) was voltage dependent and increased with depolarization, reaching a maximum average value of about 0.15 in active sweeps (500 ms steps: Fig. 3*F*), which is consistent with that previously found in lower vertebrate hair cells ($P_o = 0.24$ in 5 mM Ca^{2+}: Rodriguez-Contreras & Yamoah, 2003) and in salamander photoreceptors ($P_o = \sim 0.12$; Thoreson *et al.* 2000). The percentage of null sweeps was very high (on average > 60%) at all membrane potentials. The possibility that rapid single-channel openings were missed was excluded since no significant difference was found in the variance and the standard deviation of the current recorded in null sweeps at −67 mV and at −17 mV, which corresponds to the voltage where P_o was minimal and maximal, respectively. In contrast to our findings, a significantly higher maximal P_o and smaller elementary conductance was estimated in cochlear IHCs using ensemble variance analysis (P_o: ∼0.8; 0.62 pA at −60 mV: Brandt *et al.* 2005), which could reflect the different experimental conditions used between the two studies (e.g. extracellular Ca^{2+} concentration, age range and voltage protocol duration, which affect the possible contribution of Ca^{2+} channel inactivation).

The minimum number of Ca^{2+} channels present in pre-hearing mouse IHCs (calculated near the peak of the macroscopic I_{Ca} *I–V* curve using eqn (2) but assuming a single Ca^{2+} channel P_o of 1) is likely to be in the order of 1300 channels. However, when P_o was taken into account the total number of IHC Ca^{2+} channels was around 9600. A similar estimate of ∼11 000 channels was obtained when 5 mM or 70 mM Ba^{2+} was used as a charge carrier instead of Ca^{2+} (data not shown).

Kinetic properties of $Ca_V1.3$ Ca^{2+} channels

Fitting the dwell time distributions revealed three closed (τ_{c1}, τ_{c2} and τ_{c3}) and two open (τ_{o1} and τ_{o2}) time constants (Fig. 4). Of the three closed time constants, only τ_{c2} was clearly voltage dependent, decreasing with membrane depolarization from 16.5 ms at −67 mV to 1.9 ms at −17 mV (Fig. 4*A*). By contrast, open time constants did not change significantly with membrane depolarization (Fig. 4*B*). The relative contribution of the different closed time constants (Table 1; see also Fig. 4*C*) showed a decrease in τ_{c3} (from 50% to 4%) but an increase in τ_{c1} (from 21% to 73%) with depolarization from −67 mV to −17 mV. These data, together with a moderate increase in the relative contribution of τ_{o2} with membrane depolarization (from 5% to 21%, Fig. 4*D*), indicate an overall higher rate of

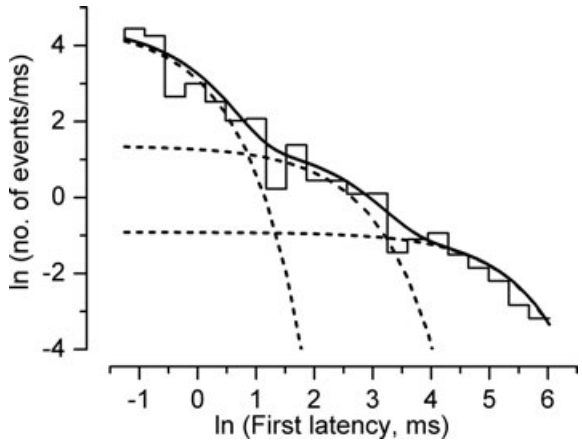

Figure 5. First latency distribution in single-channel Ca^{2+} current
First latency distribution obtained by plotting the natural logarithm of the numbers of observations per millisecond [ln(*n*/ms)] as a function of time. The continuous curved line is the third-order exponential function obtained using eqn (6). Dashed lines are the single exponential components shown separately. Fitting parameters were: $W_1 = 64.8\%$; $\tau_1 = 0.7$ ms, $W_2 = 41\%$, $\tau_2 = 10.5$ ms, $W_3 = 68.5\%$, $\tau_3 = 170.5$ ms.

transition to the channel open state. This is consistent with the increased Ca^{2+} channel P_o upon depolarization (Fig. 3*F*). The fitting parameters obtained from the open- and closed-time distribution analysis (Table 1) were used to derive the Ca^{2+} channel opening probability (Fig. 4*E*). The advantage of this alternative method, compared to that described in Fig. 3*F* (black circles), was that P_o was only estimated using the Ca^{2+} channel kinetics and therefore independent of the number of channel openings in each sweep. The very similar voltage dependence and amplitude of P_o between the plots in Fig. 3*F* (black circles) and Fig. 4*E* confirmed the very low open probability of $Ca_V1.3$ Ca^{2+} channels. More importantly, the voltage dependence of the single-channel P_o closely resembled that of the macroscopic Ca^{2+} current activation (Fig. 3*F*, grey triangles), indicating that the estimated kinetic properties of single-channel openings determine those of the whole-cell current.

The first latency (e.g. delay between the stimulus onset and first observed Ca^{2+} channel opening) was investigated in six patches showing two Ca^{2+} channels per patch. At the membrane potential of −17 mV, the distribution was best fitted by the sum of three exponentials (τ_1: 0.7 ms; τ_2: 10.5 ms; τ_3: 170.5 ms: Fig. 5). Assuming identical gating properties for both Ca^{2+} channels present in the recordings, the mean fastest single-channel latency (τ_1) is likely to be in the order of 1.4 ms. This value is significantly longer than the activation time constant measured for the ensemble average (∼0.1 ms: obtained from the same patches used for the estimation of the first latency, Fig. 3*C*) and macroscopic (∼0.3 ms, Fig. 6*D*) Ca^{2+} currents. This is likely to result from Ca^{2+} channel inactivation shortening the time at which the macroscopic Ca^{2+} current reaches the peak, which could in turn affect the estimation of its activation time constant. However, the capacitive artefact (see Methods) could have masked some initial single Ca^{2+} channel events resulting in the overestimation of the first latency, thus contributing to the above discrepancy.

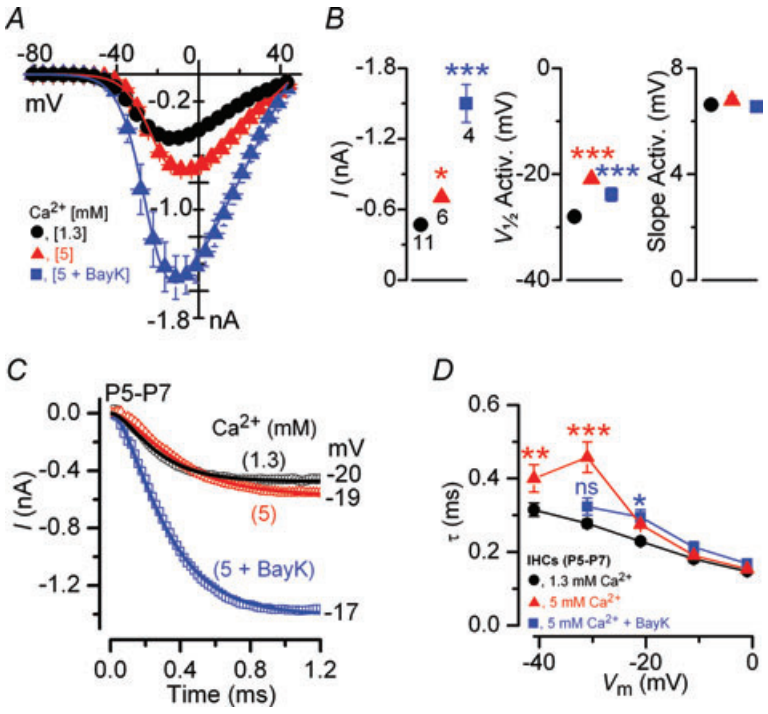

Figure 6. Biophysics of the macroscopic Ca^{2+} current in immature mouse IHCs
A, average *I–V* curves for the macroscopic I_{Ca} from P5–P7 IHCs in the presence of 1.3 mM Ca^{2+} ($n = 11$), 5 mM Ca^{2+} ($n = 6$) and 5 mM Ca^{2+} with BayK 8644 ($n = 4$). Currents were elicited by depolarizing voltage steps of 10 mV increments (10 ms in duration) from −81 mV. *B*, average maximal size (left panel), half-maximal activation ($V_{1/2}$: middle) and voltage sensitivity (*S*, right) of I_{Ca} derived from *A* using eqn (7). *C*, I_{Ca} recorded using the conditions described in *A* (first 1.2 ms). Fits to I_{Ca} activation are according to eqn (8). *D*, average I_{Ca} activation time constant (τ). Asterisks indicate significant difference when 1.3 mM Ca^{2+} was compared to 5 mM Ca^{2+} or 5 mM Ca^{2+} + BayK (*$P < 0.05$; **$P < 0.01$; ***$P < 0.001$, defined by the Tukey or Bonferroni post tests for panels *B* and *D*, respectively).

Table 1. Open (τ_o) and closed time constants (τ_c) and the relative contributions (W, %) were obtained from the exponential fits of the open and closed time distributions recorded in 5 mM Ca^{2+} at different membrane voltages

Voltage (mV)	τ_{o1} (ms)	W_{o1}	τ_{o2} (ms)	W_{o2}	τ_{c1} (ms)	W_{c1}	τ_{c2} (ms)	W_{c2}	τ_{c3} (ms)	W_{c3}
−67	0.45	94.9	4.48	5.1	0.70	20.8	16.52	28.8	107.29	50.4
−57	0.73	92.3	6.01	7.7	0.45	23.3	13.39	37.3	82.49	39.4
−47	0.44	75.4	2.83	24.6	0.48	43.4	5.42	36.4	57.59	20.2
−37	0.29	87.1	1.68	12.9	0.52	42.0	3.87	50.4	51.27	7.6
−27	0.68	85.0	2.79	15.0	0.74	68.3	3.95	28.9	83.57	2.8
−17	0.49	78.9	4.22	21.1	0.39	72.8	1.99	23.0	71.48	4.2

Although the single-channel and whole-cell measurements were performed using the same recording conditions (5 mM Ca^{2+} and BayK 8644: Fig. 3), we investigated to what extent the voltage and time dependence of the macroscopic Ca^{2+} current was affected when using 1.3 mM Ca^{2+} (the physiological perilymphatic Ca^{2+} concentration; Wangemann & Schacht, 1996) and without the gating modifier BayK 8644. The size and voltage of half-maximal activation of I_{Ca} were significantly increased when the extracellular Ca^{2+} concentration was elevated from 1.3 mM to 5 mM with or without BayK 8644 (overall: $P < 0.0001$, one-way ANOVA, for both panels *A* and *B* in Fig. 6). In particular, BayK 8644 by prolonging the single Ca^{2+} channel open time caused the amplitude of I_{Ca} to increase about 3-fold, due to an increased channel P_o. However, the voltage sensitivity of the current activation, defined by the slope factor *S*, was similar in all conditions tested (Fig. 6*B*, right panel). This indicates that the effect of BayK 8644 on $Ca_V1.3$ channel activation was not significantly voltage dependent. The activation time constant (τ) of the macroscopic Ca^{2+} current (Fig. 6*C*) was also found to be significantly smaller in 1.3 mM Ca^{2+} (overall: $P < 0.0001$, two-way ANOVA; Fig. 6*D*).

Discussion

Pre-hearing IHCs are thought to use spontaneous Ca^{2+} action potential (AP) activity to refine the wiring pattern of immature synaptic connections. The functional coding of APs largely depends on the neurotransmitter release characteristics of IHC ribbon synapses, which are under the control of $Ca_V1.3$ Ca^{2+} channels. Using the immature mouse organ of Corti, and near-physiological experimental conditions, we have presented the first biophysical description of $Ca_V1.3$ Ca^{2+} channels in native mammalian cells.

$Ca_V1.3$ Ca^{2+} channels and their role in sustaining spontaneous action potential activity in pre-hearing IHCs

The majority (>90%) of the macroscopic Ca^{2+} current in IHCs is carried by L-type Ca^{2+} channels containing the $Ca_V1.3$ subunit (Platzer *et al.* 2000). The nature of the residual Ca^{2+} current in IHCs is still unclear. In agreement with whole-cell recordings, our single-channel measurements from the basal pole region of IHCs indicated the presence of a homogeneous population of Ca^{2+} channels both in terms of current amplitude and kinetics. These biophysical properties also resembled those described in lower vertebrate hair cells from the bullfrog sacculus (Rodriguez-Contreras & Yamoah, 2001) and the chicken semicircular canal, where P/Q and N-type Ca^{2+} channel blockers were used (Zampini *et al.* 2006). $Ca_V1.3$ Ca^{2+} channels in immature IHCs can activate at a membrane potential as negative as −70 mV, indicating that they would be capable of generating spontaneous Ca^{2+} AP activity present in immature IHCs (Marcotti *et al.* 2003*b*) without the need of external depolarizing stimuli (Tritsch *et al.* 2007). The Ca^{2+} channel fastest time constant of the first latency distribution (τ_1: 1.4 ms near −20 mV) can be assumed to decrease by 20% (to ∼1.1 ms) in the presence of 1.3 mM Ca^{2+} (see Fig. 6*D*). Although the first opening delay of these Ca^{2+} channels was found to be sufficiently rapid to support the relatively slow rising phase of IHC action potentials it is unlikely to be suitable for supporting the high-frequency signalling of adult IHCs. However, recent findings have shown that the kinetics of the macroscopic Ca^{2+} current become faster in adult IHCs (Johnson & Marcotti, 2008), suggesting that some variation in the channel composition and/or their modulation is likely to occur during development.

Very few Ca^{2+} channels are associated with synaptic vesicles at IHC ribbon synapses

The number and elementary properties of $Ca_V1.3$ Ca^{2+} channels present at the presynaptic release sites of cochlear IHCs is currently unknown. We estimated that the minimum number of Ca^{2+} channels present in immature IHCs, considering the low channel P_o (0.15 at −20 mV) found in these cells, is likely to be in the order of 10 000 channels (range: 9600–11 000 channels: see Results). This is about six times larger than that previously reported using non-stationary fluctuation analysis in IHCs from young post-hearing mice (about 1800

channels: Brandt *et al*. 2005; Meyer *et al.* 2009). A few thousand Ca^{2+} channels have also been calculated using single Ca^{2+} channel recordings from lower vertebrate hair cells (∼4500 channels; Rodriguez-Contreras & Yamoah, 2001). Considering that only a small proportion (∼27%) of these 10 000 channels expressed in immature IHCs are likely to be associated with ribbons, each of the 15 active zones present in these cells (ribbons co-localized with plasma membrane Ca^{2+} channels: Fig. 1*E* and *G*) is likely to contain ∼180 Ca^{2+} channels. Therefore, we would expect an average of ∼27 Ca^{2+} channels to be simultaneously open at each IHC release site near the peak of an action potential (using a P_o of 0.15). This value can be assumed to decrease to about one-third in the presence of 1.3 mM extracellular Ca^{2+} (9 Ca^{2+} channels simultaneously open/active zone: Fig. 7), which is mainly due to a decreased channel P_o (Fig. 6). These findings indicate that, because of the low open probability, a large number (∼180) of Ca^{2+} channels per ribbon is required in order to provide, at any instant, sufficient Ca^{2+} ions to trigger vesicle fusion in the physiological voltage range (Fig. 7).

The total number of Ca^{2+} channels associated with each docked vesicle was estimated considering the size of the readily releasable pool (RRP) at each active zone, and assuming that all 180 Ca^{2+} channels are equally distributed among the vesicles in the RRP and are potentially competent for triggering their fusion. The average total RRP in an immature mouse IHC consists of ∼660 vesicles (Johnson *et al*. 2005; Khimich *et al*. 2005) equating to ∼44 vesicles fused into the membrane at around −20 mV, if equally divided among the 15 actives zones. This number would be reduced to ∼22 if docked vesicles make up only half of the RRP (Khimich *et al*. 2005). Therefore, if each vesicle is functionally coupled to Ca^{2+} channels within a nanodomain distance as recently proposed (Brandt *et al*. 2005; Moser *et al*. 2006; Goutman & Glowatzki, 2007; Johnson *et al*. 2009), then docked vesicles could be controlled by an average cluster of up to ∼4–8 Ca^{2+} channels.

Based on the Ca^{2+} channel open probability and estimated number of Ca^{2+} channels per vesicle, on average one Ca^{2+} channel per vesicle would be open 20–40% of the time at the peak Ca^{2+} current (P_o of ∼0.05: 1.3 mM Ca^{2+}), and only 1–2% of the time at around the IHC resting membrane potential (−60 mV, with a P_o of 0.003). The latter would be insufficient to cause docked vesicles to fuse at rest, which is in agreement with the fact that excitatory postsynaptic currents (EPSCs) from afferent terminals were absent when pre-hearing IHCs were voltage clamped at potentials negative to −50 mV (Goutman & Glowatzki, 2007). The above findings, together with the cooperative exocytotic Ca^{2+} dependence observed in immature IHCs (Johnson *et al*. 2005, 2009), ensures that neurotransmitter is mainly released during an action potential. However, adult auditory afferent fibres exhibit continuous resting action potential activity (Walsh & McGee, 1987) that is likely to be supported, at least in part, by the developmental linearization of the exocytotic Ca^{2+} sensitivity (Johnson *et al*. 2005; 2009), and possible changes in the elementary properties of single Ca^{2+} channels in adult IHCs.

Proposed link between Ca^{2+} channel properties and EPSCs at IHC ribbon synapses

Recordings from immature rat auditory afferent fibre terminals (Glowatzki & Fuchs, 2002; Goutman & Glowatzki, 2007) have shown a wide distribution of AMPA receptor-mediated EPSC amplitudes, with less than ten vesicles contributing to an average event, although the largest EPSCs resulted from the release of up to 20 vesicles. Such wide distribution of EPSCs has also been observed in lower vertebrate hair cell synapses (Keen & Hudspeth, 2006; Li *et al.* 2009). The rapid activation and generally monophasic appearance of the majority of such multivesicular events lead to the hypothesis that they are likely to result from the tightly coordinated fusion of docked vesicles at each IHC synaptic active zone. A

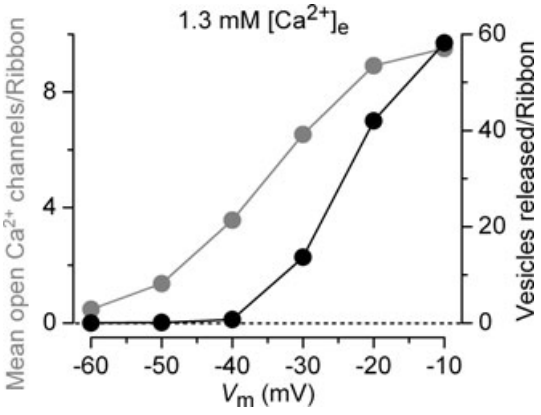

Figure 7. Mean open Ca^{2+} channels and RRP vesicles released at each IHC active zone as a function of membrane potential
The left axis indicates the mean number of open Ca^{2+} channels as a function of membrane potential obtained from $N \times P_o$, where $N = 180$ Ca^{2+} channels per ribbon synapse and P_o is that estimated in 1.3 mM extracellular Ca^{2+} from the fit in Fig. 3*F* (maximal P_o at −20 mV = 0.05: see Discussion). The right axis shows the RRP measured from ΔC_m responses in early postnatal IHCs in response to 100 ms depolarization (from Fig. 5*A* in Johnson *et al*. 2005), using a conversion factor of 37 aF per vesicle (Lenzi *et al*. 1999). The number of fused synaptic vesicles per ribbon was estimated assuming 15 active zones (see Fig. 1*G*). Note that on average, due to the very low P_o of Ca^{2+} channels, only a few of them will be open at any instant during the 100 ms depolarization (e.g. 9 Ca^{2+} channels out of 180 at −10 mV). Due to stochastic channel gating, the $[Ca^{2+}]_i$ required to release the RRP/ribbon is provided by a large number (180) of Ca^{2+} channels, each randomly opening for a small fraction of time over the 100 ms. The $[Ca^{2+}]_i$ provided by a total number of 9 Ca^{2+} channels per ribbon would be sufficient to control the RRP, instead of 180, if P_o was near to a hypothetical value of 1 (i.e. open 100% of the time).

surprising feature of the EPSCs is that their frequency, but not amplitude, increases with membrane depolarization (Goutman & Glowatzki, 2007).

The complexity of Ca^{2+} channel gating described here, with three closed and two open states (Table 1), prevents a simple correlation between channel opening and vesicle fusion at IHC ribbon synapses. For example, long lasting or bursts of short Ca^{2+} channel openings may, or may not, be equally competent to fuse a single vesicle. Nonetheless, the resemblance of EPSCs of randomly different amplitudes (Goutman & Glowatzki, 2007) to the stochastic openings of Ca^{2+} channels with different durations, suggests a possible correlation between the biophysical properties of Ca^{2+} channels and postsynaptic activity. Here we found that the single Ca^{2+} channel P_o, but not its opening time, increases steeply with membrane depolarization above −50 mV, consistent with the finding that only the frequency and not the amplitude of EPSCs increased in response to depolarizing voltage steps applied to IHCs (Goutman & Glowatzki, 2007). Therefore, it is conceivable that the wide distribution of EPSC amplitudes, which are independent of membrane depolarization (Goutman & Glowatzki, 2007), could be determined by the single-channel open time with the longest channel openings producing the largest EPSCs by facilitating the coordinate fusion of multiple vesicles at IHC release sites.

References

Beutner D & Moser T (2001). The presynaptic function of mouse cochlear inner hair cells during development of hearing. *J Neurosci* **21**, 4593–4599.

Brandt A, Khimich D & Moser T (2005). Few $Ca_V1.3$ channels regulate the exocytosis of a synaptic vesicle at the hair cell ribbon synapse. *J Neurosci* **25**, 11577–11585.

Brandt A, Striessnig J & Moser T (2003). $Ca_V1.3$ channels are essential for development and presynaptic activity of cochlear inner hair cells. *J Neurosci* **23**, 10832–10840.

Catterall WA, Perez-Reyes E, Snutch TP & Striessnig J (2005). International Union of Pharmacology. XLVIII. Nomenclature and structure-function relationships of voltage-gated calcium channels. *Pharmacol Rev* **57**, 411–425.

Colquhoun D & Hawkes AG (1987). A note on correlations in single ion channel records. *Proc R Soc Lond B Biol Sci* **230**, 15–52.

Ehret G (1975). Masked auditory thresholds, critical ratios, and scales of the basilar membrane of the housemouse (*Mus musculus*). *J Comp Physiol* **103**, 329–341.

Fettiplace R & Hackney CM (2006). The sensory and motor roles of auditory hair cells. *Nat Rev Neurosci* **7**, 19–29.

Fuchs PA (2005). Time and intensity coding at the hair cell's ribbon synapse. *J Physiol* **566**, 7–12.

Glowatzki E & Fuchs PA (2002). Transmitter release at the hair cell ribbon synapse. *Nat Neurosci* **5**, 147–154.

Glowatzki E, Grant L & Fuchs PA (2008). Hair cell afferent synapses. *Curr Opin Neurobiol* **18**, 389–395.

Goutman JD & Glowatzki E (2007). Time course and calcium dependence of transmitter release at a single ribbon synapse. *Proc Natl Acad Sci U S A* **104**, 16341–16346.

Grant L & Fuchs PA (2008). Calcium- and calmodulin-dependent inactivation of calcium channels in inner hair cells of the rat cochlea. *J Neurophysiol* **99**, 2183–2193.

Hackney CM, Mahendrasingam S, Penn A & Fettiplace R (2005). The concentration of calcium buffering proteins in mammalian cochlear hair cells. *J Neurosci* **25**, 7867–7886.

Hess P, Lansman JB & Tsien RW (1984). Different modes of Ca^{2+} channel gating behaviour favoured by dihydropyridine Ca^{2+} agonists and antagonists. *Nature* **311**, 538–544.

Hodgkin AL & Huxley AF (1952). A quantitative description of membrane current and its application to conduction and excitation in nerve. *J Physiol* **117**, 500–544.

Johnson SL, Adelman JP & Marcotti W (2007). Genetic deletion of SK2 channels in mouse inner hair cells prevents the developmental linearization in the Ca^{2+} dependence of exocytosis. *J Physiol* **583**, 631–646.

Johnson SL, Forge A, Knipper M, Münkner S & Marcotti W (2008). Tonotopic variation in the calcium dependence of neurotransmitter release and vesicle pool replenishment at mammalian auditory ribbon synapses. *J Neurosci* **28**, 7670–7678.

Johnson SL, Franz C, Knipper M & Marcotti W (2009). Functional maturation of the exocytotic machinery at gerbil hair cell ribbon synapses. *J Physiol* **587**, 1715–1726.

Johnson SL & Marcotti W (2008). Biophysical properties of $Ca_V1.3$ calcium channels in gerbil inner hair cells. *J Physiol* **586**, 1029–1042.

Johnson SL, Marcotti W & Kros CJ (2005). Increase in efficiency and reduction in Ca^{2+} dependence of exocytosis during development of mouse inner hair cells. *J Physiol* **563**, 177–191.

Keen EC & Hudspeth AJ (2006). Transfer characteristics of the hair cell's afferent synapse. *Proc Natl Acad Sci U S A* **103**, 5537–5542.

Khimich D, Nouvian R, Pujol R, tom Dieck S, Egner A, Gundelfinger ED & Moser T (2005). Hair cell synaptic ribbons are essential for synchronous auditory signalling. *Nature* **434**, 889–894.

Knipper M, Zinn C, Maier H, Praetorius M, Rohbock K, Köpschall I & Zimmermann U (2000). Thyroid hormone deficiency before the onset of hearing causes irreversible damage to peripheral and central auditory systems. *J Neurophysiol* **83**, 3101–3112.

Knirsch M, Brandt N, Braig C, Kuhn S, Hirt B, Munkner S, Knipper M & Engel J (2007). Persistence of $Ca_V1.3$ Ca^{2+} channels in mature outer hair cells supports outer hair cell afferent signalling. *J Neurosci* **27**, 6442–6451.

Kros CJ, Ruppersberg JP & Rüsch A (1998). Expression of a potassium current in inner hair cells during development of hearing in mice. *Nature* **394**, 281–284.

Lenzi D, Runyeon JW, Crum J, Ellisman MK & Roberts WM (1999). Synaptic vesicle populations in saccular hair cells reconstructed by electron tomography. *J Neurosci* **19**, 119–132.

Li GL, Keen E, Andor-Ardó D, Hudspeth AJ & von Gersdorff H (2009). The unitary event underlying multiquantal EPSCs at a hair cell's ribbon synapse. *J Neurosci* **29**, 7558–7568.

McManus OB, Blatz AL & Magleby KL (1987). Sampling, log binning, fitting, and plotting durations of open and shut intervals from single channels and the effects of noise. *Pflugers Arch* **410**, 530–553.

Marcotti W, Johnson SL, Holley MC & Kros CJ (2003*a*). Developmental changes in the expression of potassium currents of embryonic, neonatal and mature mouse inner hair cells. *J Physiol* **548**, 383–400.

Marcotti W, Johnson SL & Kros CJ (2004). A transiently expressed SK current sustains and modulates action potential activity in immature mouse inner hair cells. *J Physiol* **560**, 691–708.

Marcotti W, Johnson SL, Rüsch A & Kros CJ (2003*b*). Sodium and calcium currents shape action potentials in immature mouse inner hair cells. *J Physiol* **552**, 743–761.

Meyer AC, Frank T, Khimich D, Hoch G, Riedel D, Chapochnikov NM, Yarin YM, Harke B, Hell SW, Egner A & Moser T (2009). Tuning of synapse number, structure and function in the cochlea. *Nat Neurosci* **12**, 444–453.

Moser T, Neef A & Khimich D (2006). Mechanisms underlying the temporal precision of sound coding at the inner hair cell ribbon synapse. *J Physiol* **576**, 55–62.

Neef A, Khimich D, Pirih P, Riedel D, Wolf F & Moser T (2007). Probing the mechanism of exocytosis at the hair cell ribbon synapse. *J Neurosci* **27**, 12933–12944.

Platzer J, Engel J, Schrott-Fischer A, Stephan K, Bova S, Chen H, Zheng H & Striessnig J (2000). Congenital deafness and sinoatrial node dysfunction in mice lacking class D L-type Ca^{2+} channels. *Cell* **102**, 89–97.

Plummer MR, Logothetis DE & Hess P (1989). Elementary properties and pharmacological sensitivities of calcium channels in mammalian peripheral neurons. *Neuron* **2**, 1453–1463.

Prigioni I, Masetto S, Russo G & Taglietti V (1992) Calcium currents in solitary hair cells isolated from frog crista ampullaris. *J Vestib Res* **2**, 31–39.

Pujol R, Lavigne-Rebillard M & Lenoir M (1998). Development of sensory and neural structures in the mammalian cochlea. In *Development of the Auditory System*, ed. Rubel EW, Popper AN & Fay RR, pp. 146–192. Springer, New York.

Regus-Leidig S, Dieck T, Specht D, Meyer L & Brandstatter JH (2009) Early steps in the assembly of photoreceptor ribbon synapses in the mouse retina: the involvement of precursor spheres. *J Comp Neurol* **512**, 814–824.

Roberts WM (1993). Spatial calcium buffering in saccular hair cells. *Nature* **363**, 74–76.

Rodriguez-Contreras A & Yamoah EN (2001). Direct measurement of single-channel Ca^{2+} currents in bullfrog hair cells reveals two distinct channel subtypes. *J Physiol* **534**, 669–689.

Rodriguez-Contreras A & Yamoah EN (2003). Effects of permeant ion concentrations on the gating of L-type Ca^{2+} channels in hair cells. *Biophys J* **84**, 3457–3469.

Russo G, Lelli A, Gioglio L & Prigioni I (2003). Nature and expression of dihydropyridine-sensitive and -insensitive calcium currents in hair cells of frog semicircular canals. *Pflugers Arch* **446**, 189–197.

Sigworth FJ & Sine SM (1987). Data transformations for improved display and fitting of single-channel dwell time histograms. *Biophys J* **52**, 1047–1054.

Sobkowicz HM, Rose JE, Scott GE & Slapnick SM (1982). Ribbon synapses in the developing intact and cultured organ of Corti in the mouse. *J Neurosci* **2**, 942–957.

Sterling P & Matthews G (2005). Structure and function of ribbon synapses. *Trends Neurosci* **28**, 20–29.

Thoreson WB, Nitzan R & Miller RF (2000). Chloride efflux inhibits single calcium channel open probability in vertebrate photoreceptors: chloride imaging and cell-attached patch-clamp recordings. *Vis Neurosci* **17**, 197–206.

Tritsch NX, Yi E, Gale JE, Glowatzki E & Bergles DE (2007). The origin of spontaneous activity in the developing auditory system. *Nature* **450**, 50–55.

Walsh EJ & McGee J (1987). Postnatal development of auditory nerve and cochlear nucleus neuronal responses in kittens. *Hear Res* **28**, 97–116

Wangemann P & Schacht J (1996). Homeostatic mechanisms in the cochlea. In *The Cochlea*, ed. Dallos P, Popper AN & Fay RR, pp. 139–185. Springer, New York.

Wittig JH & Parsons TD (2008). Synaptic ribbon enables temporal precision of hair cell afferent synapse by increasing the number of readily releasable vesicles: a modelling study. *J Neurophysiol* **100**, 1724–1739.

Zampini V, Valli P, Zucca G & Masetto S (2006). Single-channel L-type Ca^{2+} currents in chicken embryo semicircular canal type I and type II hair cells. *J Neurophysiol* **96**, 602–612.

Zidanic M & Fuchs PA (1995). Kinetic analysis of barium currents in chick cochlear hair cells. *Biophys J* **68**, 1323–1336.

Author contributions

V.Z. and S.L.J. collected the electrophysiological data (in the UK). C.F. and M.K. performed the immuno-labelling experiments (in Germany). All authors were involved in study design, data analysis and interpretation. W.M. conceived and coordinated the study, participated in data collection and wrote the paper together with S. Masetto. All authors discussed the results, commented on the manuscript and approved the version to be published.

Acknowledgements

This work was supported by grants from the Wellcome Trust, Deafness Research UK and The Royal Society to W.M.; the Ministero della Università e della Ricerca to S. Masetto; DFG 316-4-1 and by the European Union Research Programme 6th FP MRTN-CT-2006-035367 to M.K. V.Z. was supported by The Royal Society Short Incoming Visit grant to W.M. W.M. is a Royal Society University Research Fellow. We would like to thank R. Fettiplace and A. Ricci for their comments on an earlier version of the manuscript. We would also like to thank E. Dalhoff for advice regarding the resolution of the optical system used for immunolabelling experiments and M. Cardwell for his excellent assistance with the animals.